RMetS
Royal Meteorological Society

Dynamical Core Model Intercomparison Project (DCMIP) tracer transport test results for CAM-SE

David M. Hall,[a]* Paul A. Ullrich,[b] Kevin A. Reed,[c] Christiane Jablonowski,[d] Ramachandran D. Nair[e]† and Henry M. Tufo[a]

[a]*Department of Computer Science, University of Colorado, Boulder, USA*
[b]*Department of Land, Air, and Water Resources, University of California, Davis, USA*
[c]*School of Marine and Atmospheric Sciences, Stony Brook University, NY, USA*
[d]*Department of Climate and Space Sciences and Engineering, University of Michigan, Ann Arbor, USA*
[e]*National Center for Atmospheric Research, Boulder, CO, USA*

*Correspondence to: D. M. Hall, Department of Computer Science, University of Colorado Boulder, 1045 Regent Drive 430 UCB, Boulder, CO 80309-0430, USA. E-mail: david.hall@colorado.edu

The Dynamical Core Model Intercomparison Project (DCMIP) provides a set of tests and procedures designed to facilitate development and intercomparison of atmospheric dynamical cores in general circulation models (GCMs). Test category 1 examines the advective transport of passive tracers by three-dimensional prescribed wind velocity fields, on the sphere. These tests are applied to the Spectral Element (SE) dynamical core of the Community Atmosphere Model (CAM), the default for high-resolution simulations in the Community Earth System Model (CESM). Test case results are compared with results from the CAM-FV (Finite Volume) and MCore models where possible. This analysis serves both to evaluate the performance of CAM-SE's spectral-element tracer transport routines as well as to provide a baseline for comparison with other atmospheric dynamical cores and for future improvements to CAM-SE itself.

Key Words: DCMIP; CAM-SE; atmosphere model; tracer transport; dynamical core; model intercomparison; climate modeling; spectral elements

Received 24 April 2015; Revised 20 November 2015; Accepted 1 February 2016; Published online in Wiley Online Library

1. Introduction

The Dynamical Core Model Intercomparison Project organized by Jablonowski *et al.* (2012) is an international collaboration tasked with producing a set of standardized benchmarks for intercomparison of atmospheric dynamical cores in global climate models. The DCMIP tests are designed to supplement existing model intercomparison suites including the shallow-water test cases of Williamson *et al.* (1992), the Atmospheric Model Intercomparison (AMIP) tests of Gates (1992) and Gates *et al.* (1999), and the Coupled Model Intercomparison Project (CMIP) tests of Meehl *et al.* (2000, 2005). The DCMIP tests focus solely on the atmospheric dynamical core in isolation from other model components, covering the intermediate regime between shallow-water simulations and 3D global simulations with full physics. They are intended to be of particular value in the early stages of model development and in the development of non-hydrostatic atmospheric dynamical cores.

In this article, the DCMIP tracer transport tests are applied to the spectral element dynamical core of the Community Atmosphere Model, subsequently referred to as CAM-SE. As described in Dennis *et al.* (2012), CAM-SE is the current default spectral-element atmospheric dynamical core of the Community Earth System Model (CESM) for high-resolution simulations. Improvement of CAM-SE is an area of active research, with projects spanning the development of non-hydrostatic models, improved vertical representations, a discontinuous-Galerkin discretization, fully implicit and semi-implicit time discretizations, amongst others. The main purpose of this article is to establish a baseline set of results, in order to facilitate objective analysis of new technologies within CAM-SE. Due to space constraints, this article focuses solely on the tracer transport tests, with the remainder of the DCMIP test suite left for future publication.

As DCMIP represents a new protocol, only a handful of results have been published to date. The details of each DCMIP test and its recommended usage are described at length in Ullrich *et al.* (2012). The tracer transport tests were presented in further detail in Kent *et al.* (2014) along with sample test results for the CAM-FV and MCore dynamical cores (Ullrich and Jablonowski, 2012). These tests were also used in Nair *et al.* (2015). The most complete description of the DCMIP test suite is provided by the project website (Jablonowski *et al.*, 2012) where test descriptions, Fortran code, and sample results for many different models, both hydrostatic and non-hydrostatic, are available. To date, more than

15 modelling groups have contributed to the intercomparison by running many of the tests from the DCMIP suite. However, while useful, the online results for most models are incomplete and could benefit from further analysis.

DCMIP category 1 consists of three passive tracer advection tests which are three-dimensional generalizations of well-known two-dimensional test cases. DCMIP test 1-1 applies a highly deformational lateral velocity field, and is based on the deformational test case 4 of Nair and Lauritzen (2010). DCMIP 1-1 differs from that test in that an oscillatory vertical transport component has been added to make it fully three-dimensional. Also two tracer fields with a specific nonlinear relationship were added to enable application of the tracer-correlation diagnostics described in Lauritzen and Thuburn (2012). DCMIP test 1-2 produces a Hadley-like meridional circulation and is designed to test the accuracy of the coupling between the horizontal and vertical representations. It is a generalization of the test described in Zerroukat and Allen (2012) with time-reversal added to provide an analytical solution for error analysis. DCMIP test 1-3 examines the advection of tracers over steep orography. It is an extension of the 2D test in the x–z plane of Schär *et al.* (2002), with thin-cloud layers placed at multiple heights in order to evaluate the effects of terrain-following coordinates.

The remainder of this article is organized as follows. Section 2 reviews aspects of the CAM-SE model relevant to tracer transport including the computational mesh, the tracer transport algorithm, and regularization. In section 3, the DCMIP 1-x tests are described and results are presented for the CAM-SE dynamical core. In section 4, the results are summarized.

2. The CAM-SE model

The Community Earth System Model described in Hurrell *et al.* (2013) is a freely distributed global climate model with a large community of users. It is composed of multiple components representing the atmosphere, ocean, land, ice and other geophysical subsystems of the global Earth system. Its atmospheric component CAM is described in detail in Neale *et al.* (2010). CAM is composed of a dynamical core and a physical parametrization package. The dynamical core is responsible for simulating the geophysical fluid flow explicitly resolved at a given resolution. The physics package parametrizes important physical processes occurring on sub-grid scales not explicitly resolved by the model such as atmospheric turbulence, radiative transfer, convection, and boundary-layer processes.

CAM may be configured to use one of several distinct dynamical cores including CAM-SE, CAM-FV, CAM-EUL, or CAM-SLD. The default dynamical core for high-resolution simulations is CAM-SE, which employs a split spatial representation with a fourth-order accurate spectral-element discretization in the horizontal and second-order accurate floating-Lagrangian and finite-difference (FD) discretizations in the vertical. CAM-SE represents one of several models developed in HOMME, the High-Order Method Modeling Environment, first introduced by Thomas and Loft (2005). The DCMIP 1-x tests described herein were executed in the HOMME stand-alone environment.

In the following sections, the CAM-SE routines relevant for tracer transport are summarized. Neale *et al.* (2010) and Dennis *et al.* (2012) give a more complete description of the CAM-SE atmospheric dynamical core.

2.1. The computational mesh

CAM-SE makes use of a hybrid pressure terrain-following vertical coordinate η described in Simmons and Burridge (1981). The pressure p is related to η through the hybrid coefficients $A(\eta)$ and $B(\eta)$ such that $p(\lambda,\varphi,\eta) = A(\eta)p_0 + B(\eta)p_s(\lambda,\varphi)$, where $\eta = A(\eta) + B(\eta)$ lies in the range $\eta \in [0,1]$, the quantity $p_0 = 1000\,\text{hPa}$ is a constant reference pressure, and $p_s(\lambda,\varphi)$ is the surface pressure. The DCMIP tracer transport tests employ coefficients with the analytic relationship

$$B_i = \left[\frac{\eta_i - \eta_t}{1-\eta_t}\right]^c, \qquad A_i = \eta_i - B_i\,, \tag{1}$$

where c is a smoothing exponent that controls the rate at which η transforms from a terrain-following coordinate to a pure pressure coordinate at the upper boundary η_t. Unless otherwise noted, $c = 1$ is used as the default. Default operational values of the A and B coefficients used in CAM-SE may be found in Appendix B of Reed and Jablonowski (2012).

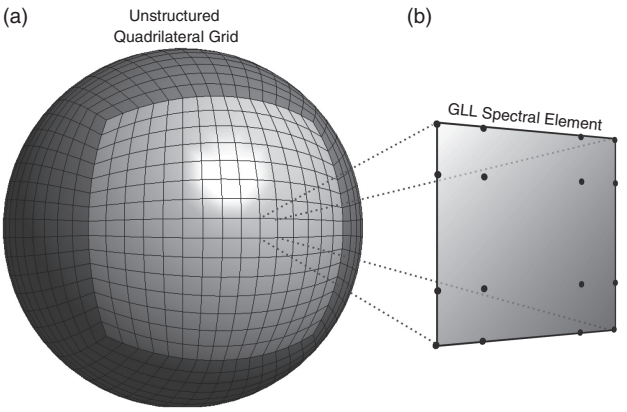

Figure 1. (a) Horizontal discretization CAM-SE employs an unstructured grid of curvilinear quadrilateral elements, arranged in a cubed-sphere configuration by default with N_e elements per face by default. (b) Scalar fields are represented by polynomials with N_p nodes, or degrees of freedom per element edge. The nodes are placed at Gauss–Lobatto–Legendre (GLL) quadrature points to simplify numerical integration and to diagonalize the elemental mass matrix. In this example, $N_e = 15$ and $N_p = 4$ which corresponds to a mean spacing of 2° per degree of freedom.

In the horizontal, CAM-SE partitions the domain into an unstructured mesh of non-overlapping quadrilateral elements with conforming edges. Elements are arranged in a cubed-sphere configuration by default, as shown in Figure 1(a). A cubed-sphere mesh, first introduced by Sadourny (1972), is advantageous as its elements are quasi-uniform in size, and it avoids element clustering at the poles, which plagues the traditional longitude–latitude grid. Each cube face is divided into N_e elements per edge which are mapped to the surface of the sphere using the gnomonic equal-angle projection of Rančić *et al.* (1996).

2.2. Tracer transport

The tracer transport routine in CAM-SE employs a discrete version of the advection equation

$$\frac{\partial}{\partial t}\left(q_i\frac{\partial p}{\partial \eta}\right) + \nabla_\eta\cdot\left(q_i\mathbf{u}\frac{\partial p}{\partial \eta}\right) + \frac{\partial}{\partial \eta}\left(q_i\dot{\eta}\,\frac{\partial p}{\partial \eta}\right) = 0, \tag{2}$$

expressed in η vertical coordinates, following Simmons and Burridge (1981) using the generalized vertical transforms of Kasahara (1974). The quantity q_i represents the mixing ratio of a given tracer i, and $\dot{\eta}$ is the vertical velocity in η coordinates. The vertical pressure gradient $\partial p/\partial\eta$ acts a pseudo-density and is related to the true density ρ by the hydrostatic balance condition $\partial p/\partial\eta = -g\rho\partial z/\partial\eta$. Other model quantities are defined in Table 1. Lateral and vertical tracer transport are performed separately in a time-split manner, using the spectral element method in the horizontal followed by a Lagrangian method in the vertical.

Vertical transport is accomplished using the Lagrangian approach of Lin (2004). The tracers are transported using a Lagrangian coordinate system η' moving with the tracers such that $\dot{\eta}' = 0$. At the beginning of each time step, the η' levels coincide with η-level midpoints. After several tracer time steps, the tracers are mapped back onto the η-layer midpoints using a

Table 1. Model variable definitions.

f	Coriolis parameter
$\widehat{\mathbf{k}}$	radial unit vector
L	number of vertical levels
p	pressure
p_s	surface pressure
q_i	tracer mixing ratio
t	time
T	temperature
u	zonal wind
$\mathbf{u} = (u, v)$	lateral wind vector
v	meridional wind
w	vertical velocity
η	hybrid vertical coordinate
λ	longitude
ρ	density
$\Phi = gz$	geopotential
φ	latitude
ω	vertical pressure velocity
Δx	mean horizontal resolution
lim	limiter option

monotone remapping technique, similar to the one described in Nair *et al.* (2009).

Horizontal transport is accomplished by applying the nodal spectral element method to solve the discrete form of

$$\frac{\partial}{\partial t}\left(q_i\widetilde{\rho}\right) = -\nabla\cdot\left(q_i\widetilde{\rho}\,\mathbf{u}\right), \tag{3}$$

where $\widetilde{\rho} = \partial p/\partial\eta'$ is the pseudo-density in η' coordinates.

Alternative horizontal tracer transport schemes based on semi-Lagrangian techniques are available in CAM, including the CSLAM method of Lauritzen *et al.* (2010) and the SPELT method of Erath and Nair (2014). However, this discussion will be limited to the default transport scheme.

The tracer transport equations are discretized in time using a three-stage strong-stability-preserving (SSP) second-order accurate Runge–Kutta (RK) method of Spiteri and Ruuth (2002). This method was chosen to preserve horizontal monotonicity. In CAM-SE, the horizontal tracer-transport routines are sub-cycled n_r times between vertical re-mapping events, and dynamics routines are sub-cycled n_q times per tracer-transport step. In this work, $n_r = 1$, indicating that remapping is applied after each tracer transport step, and the value of n_q is unspecified as the remaining dynamics routines are not used.

2.3. The projection operator

The spectral element method requires globally continuous solutions. After a single time step, the solution will in general be discontinuous at element edges, as only data within a given element are used to compute the local solution. To restore continuity, a projection operator $\mathcal{P} : \mathcal{V}^0 \rightarrow \mathcal{V}^1$ must be applied, where $\mathcal{V}^0$ is the space of piecewise continuous polynomials spanned by ϕ_i and $\mathcal{V}^1$ is the subset of those that are also $\mathcal{C}^0$ continuous.

In practice, this operation is performed by averaging the values at GLL nodes shared by more than one element. This process is referred to as global assembly in Karniadakis and Sherwin (2013) or as the direct stiffness summation (DSS) in Deville *et al.* (2002). The DSS projection is applied after each sub-step of the RK time integration.

2.4. Regularization

The solution produced by time-integration of the tracer transport equation is accurate and locally conservative but it can also be oscillatory. Various optional limiters may be applied after the remap phase in order to reduce or eliminate oscillations and to prevent non-positive tracer values, as discussed in Taylor *et al.* (2009). By default, CAM-SE uses an optimization based quasi-monotone limiter applied to the tracer mass field $q_i\Delta p$ as described in Guba *et al.* (2014). This limiter is employed in each of the tests below, unless otherwise noted.

A horizontal hyperviscosity operator may be applied after each tracer advection step to smooth the solution, using

$$\frac{\partial q_i}{\partial t} = -\nu\,\nabla^4 q_i\,, \tag{4}$$

where ν is the adjustable hyperviscosity coefficient. In practice, it is applied in a two-stage process that uses only first derivatives. In the first step, an auxiliary variable $f_i = \nabla\cdot(\nabla q_i)$ is constructed using the discrete forms of the gradient ∇ and divergence $\nabla\cdot$ operators. The tracer field is then updated as follows:

$$q_i(t+\Delta t) = q_i(t) - \Delta t\,\nu\,\nabla\cdot(\nabla f_i). \tag{5}$$

The hyperviscosity may also be sub-cycled, but for the test cases presented here, when hyperviscosity is used, it is applied only once per time step.

Table 2. Parameters for 3D deformation test 1-1.

Parameter	Value	Description
a	6.37122×10^6 m	Radius of the Earth
g	9.80616 m s^{-2}	Gravity
H	$R_dT_0/g = 8.78$ km	Scale height
k	$10a/\tau$	Deformational wind speed
p_0	1000 hPa	Reference pressure
R_d	287.0 J kg^{-1}K^{-1}	Gas constant for dry air
T_0	300 K	Isothermal temperature
z_t	12 000 m	z coordinate of model top
η_t	0.255	η coordinate of model top
λ'	$\lambda - 2\pi t/\tau$	Translational longitude
τ	12 days	Period of motion
Φ_s	0	Flat geopotential surface

3. DCMIP tests and results

DCMIP category 1 describes three tracer transport scenarios in which analytic time-dependent wind velocity fields are prescribed and all other dynamics routines are disabled. Each test concludes by returning the tracers to their initial positions, in order to provide an analytical solution for error analysis. Test output is produced following the recommended usage and diagnostics described in the DCMIP Test Case Document of Ullrich *et al.* (2012) together with additional analysis, where relevant. Some example results were presented in Kent *et al.* (2014) using the CAM-FV and MCore finite-volume dynamical cores. In the following analysis, output from CAM-SE is compared with the CAM-FV and MCore models whenever possible.

3.1. DCMIP test 1-1: 3D deformational flow

3.1.1. Test case description

DCMIP test 1-1 examines the transport of passive tracers in a three-dimensional, deformational flow. It is based on two-dimensional tests introduced by Nair and Lauritzen (2010), with an additional vertical wind component. It uses an isothermal temperature field with $T = 300$ K throughout with an exponential pressure distribution

$$p = p_0\exp(-z/H), \tag{6}$$

$$\rho = p/(R_dT), \tag{7}$$

with constant scale height $H = R_dT_0/g$. The density ρ is given by the ideal gas law for dry air, and the surface geopotential $\Phi_s = 0$ is flat. Other test parameters are summarized in Table 2.

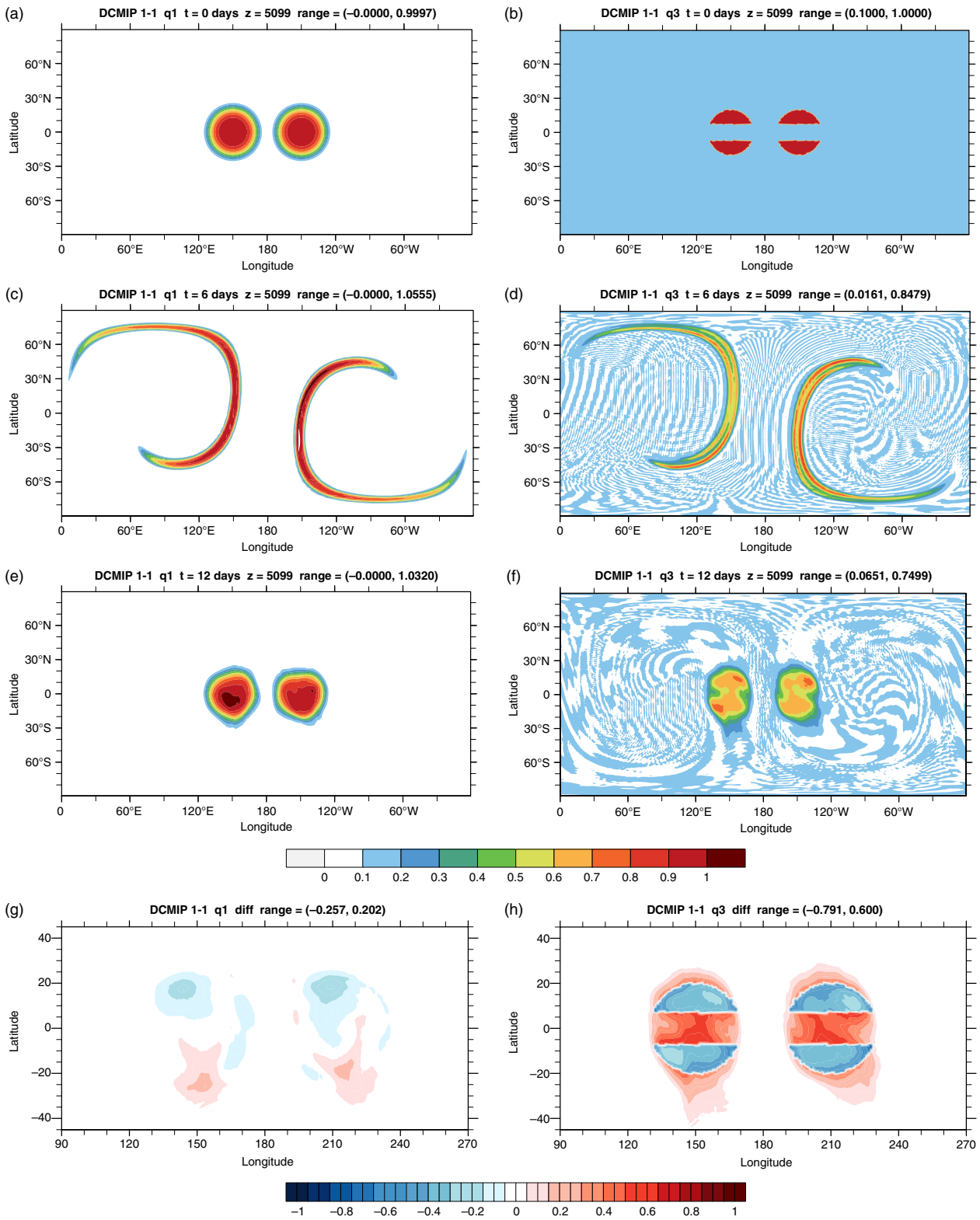

Figure 2. DCMIP 1-1 horizontal cross-sections of tracers (a, c, e, g) q_1 and (b, d, f, h) q_3 as a function of time. Snapshots are taken at (a, b) $t = 0$ days, (c, d) 6 days and (e, f) $t = 12$ days. (g, h) show the differences between the final and initial states. [$\Delta x = 1^\circ, N_e = 30, N_p = 4, L = 60, \Delta t = 100$ s, $\nu = 0$ m^{4}s^{-1}, $z = 5100$ m, quasi-monotone limiter.]

Prescribed winds are applied over twelve model days with a sinusoidal time dependence that reverses at day 6. The wind fields are composed of a horizontally deformational component $\mathbf{u}_a$ and a horizontally divergent component $\mathbf{u}_d$ such that $\mathbf{u} = \mathbf{u}_a + \mathbf{u}_d$ where

$$u_a = k \sin^2 \lambda' \sin(2\varphi) \cos(\pi t/\tau) + (2\pi a/\tau) \cos\varphi, \quad (8)$$

$$v_a = k \sin(2\lambda') \cos\varphi \cos(\pi t/\tau), \quad (9)$$

$$u_d = (\omega_0 a / b p_t) \cos\lambda' \cos^2\varphi \cos(2\pi t/\tau)\, s_2(p), \quad (10)$$

$$v_d = 0. \quad (11)$$

The vertical velocity in hybrid η coordinates is

$$\dot{\eta} = (\omega_0/p_0) \sin\lambda' \cos\varphi \cos(2\pi t/\tau)\, s_1(p), \quad (12)$$

where $s_1(p)$ and $s_2(p)$ are shape functions:

$$s_1(p) = 1 - \exp\left(\frac{p-p_0}{bp_t}\right) - \exp\left(\frac{p_t-p}{bp_t}\right) + \exp\left(\frac{p_t-p_0}{bp_t}\right),$$

$$s_2(p) = -\exp\left(\frac{p-p_0}{bp_t}\right) + \exp\left(\frac{p_t-p}{bp_t}\right). \quad (13)$$

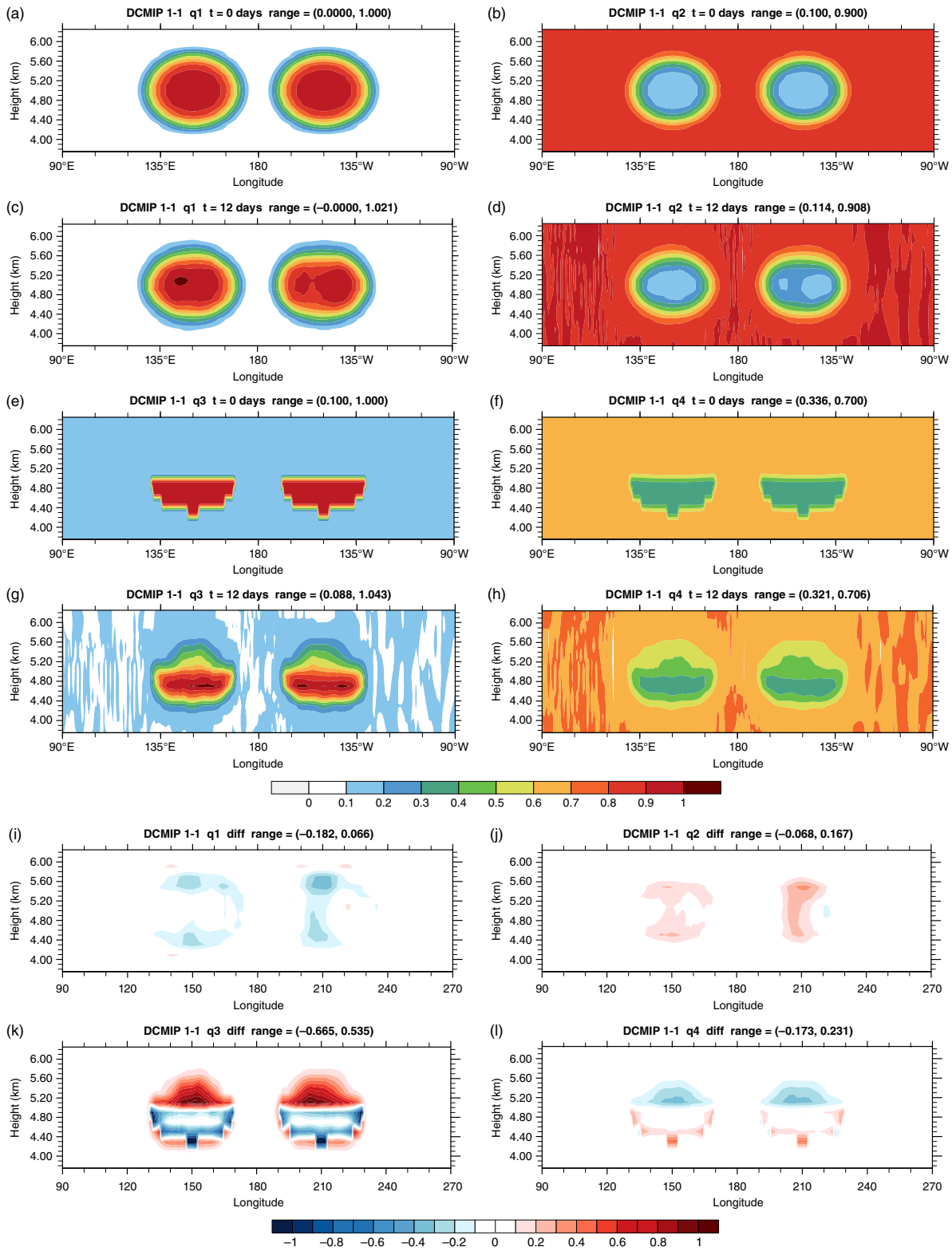

Figure 3. DCMIP 1-1 vertical cross-sections through all four tracer fields (a, c) q_1, (b, d) q_2, (e, g) q_3, and (f, h) q_4 at the Equator, at time (a, b, e, f) $t = 0$ and (c, d, g, h) $t = 12$ days. (i)–(l) show their difference fields. [$\Delta x = 1°$, $N_e = 30$, $N_p = 4$, $L = 60$, $\Delta t = 100$ s, $\nu = 0$ m^{4}s^{-1}, quasi-monotone limiter.]

The function $s_1(p)$ tapers the vertical velocity to 0 at the top and bottom of the computational domain.

Tracer mixing ratios are initialized as follows:

$$q_1 = 0.5\{1 + \cos(\pi d_1)\} + 0.5\{1 + \cos(\pi d_2)\}, \tag{14}$$

$$q_2 = 0.9 - 0.8\, q_1^2, \tag{15}$$

$$q_3 = \begin{cases} 1 & \text{if } d_1 < \frac{1}{2} \text{ or } d_2 < \frac{1}{2}, \\ 0.1 & \text{if } z > z_c \text{ and } \varphi_c - \frac{1}{8} < \varphi < \varphi_c + \frac{1}{8}, \\ 0.1 & \text{otherwise,} \end{cases} \tag{16}$$

$$q_4 = 1 - \frac{3}{10}\left(q_1 + q_2 + q_3\right). \tag{17}$$

Tracer q_1 is assigned a smooth, double cosine bell pattern where d_i is a scaled distance function as specified in Kent *et al.* (2014). Tracer q_2 is chosen to assess the ability of the scheme to maintain a nonlinear relationship with tracer q_1. Tracer q_3 is composed of two slotted ellipses centered at latitude φ_c and altitude z_c, and is designed to assess the capability of the transport scheme to maintain monotonicity. Tracer q_4 is chosen to investigate whether a linear sum of tracers can be maintained by the transport scheme.

The test employs 60 vertical levels with evenly spaced z coordinates ranging in height from 0 to 12 000 m with $\Delta z =$ 200 m. Hybrid η levels are then assigned to be $\eta = \exp(-z/H)$ using Eq. (6). The horizontal resolution for each simulation is set to $N_p = 4, N_e = 30$ (fourth-order polynomials with 30 elements

Table 3. DCMIP 1-1 error norms for tracer fields at $t = 12$ days. CAM-SE simulation parameters. [$\Delta x = 1^\circ, N_p = 4, N_e = 30, L = 60, \Delta t = 100$ s, $\nu = 0\,\mathrm{m}^4\,\mathrm{s}^{-1}$, quasi-monotone limiter.]

Model	Norm	q_1	q_3	q_4
CAM-SE	ℓ_1	0.1813	0.0241	0.0013
	ℓ_2	0.1518	0.2260	0.0117
	ℓ_∞	0.3198	0.8162	0.3673
CAM-FV	ℓ_1	0.1210	0.0236	0.0011
	ℓ_2	0.0998	0.2519	0.0130
	ℓ_∞	0.1923	0.8589	0.3990
MCore	ℓ_1	0.1774	0.0251	0.0014
	ℓ_2	0.1552	0.2354	0.0125
	ℓ_∞	0.3384	0.8444	0.3906

per cube-face) unless otherwise specified. This corresponds to an average resolution of 1.0° (110 km) per node at the Equator. Simulations were performed without hyperviscosity $\nu = 0\,\mathrm{m}^4\,\mathrm{s}^{-1}$ using a time step of $\Delta t = 100$ and the default quasi-monotonic limiter.

3.1.2. *DCMIP 1-1 tracer cross-sections*

Figure 2 displays horizontal cross-sections of tracer fields q_1 and q_3 at a height of 5100 m (level 34 of 60 from the top) plotted at time $t = 0$, 6 and 12 days. At the bottom of the figure, tracer errors $\delta q_i = q_i(\tau) - q_i(0)$ are produced by subtracting the final state from the initial state. Areas of excess tracer are shaded red and areas with a tracer deficit are shaded blue. The maximum and minimum values of δq_i within the cross-section are also displayed. Note that all results have been interpolated from CAM-SE's native spectral-element grid to a uniform longitude–latitude grid for visualization.

We observe that, even after significant stretching and shearing, the general horizontal shape of the smooth tracers field q_1 is reasonably well preserved, with some latitudinal elongation. The q_3 tracer distribution also retains its slotted-cylinder shape at the final time although with significant smoothing, producing areas of excess tracer concentration in the central slot.

Small-amplitude oscillations are clearly visible in the solution for tracer q_3 at times $t = 6$ and $t = 12$ despite the use of the quasi-monotone limiter. This loss of monotonicity in the mixing ratio is most likely due to wind–mass inconsistency that commonly arises in prescribed velocity scenarios, as discussed in Jöckel *et al.* (2001) and Nair and Lauritzen (2010). While the limiter ensures monotonicity of the tracer mass $q_i \Delta p$, it does not guarantee the monotonicity of the tracer mixing ratio $q_i = (q_i \Delta p)/\Delta p_a$ due to inconsistencies between the analytic value Δp_a and numerical value of Δp.

Figure 3 displays vertical cross-sections of the tracer fields at the Equator at $t = 0$ and the final time, $t = 12$ days. Difference fields are plotted at the bottom of the figure. As with the horizontal cross-sections, the general shape and features of each tracer distribution is maintained at the final time but with significant smoothing of sharp features.

3.1.3. *DCMIP 1-1 error norms*

Error norms are computed for each tracer by comparing its final state q_τ to its initial state q_0 and applying the following definitions for the ℓ_1, ℓ_2, and ℓ_∞ norms

$$\ell_1(q) = I\left[|q_\tau - q_0|\right] / I[|q_0|], \tag{18}$$

$$\ell_2(q) = \sqrt{I\left[(q_\tau - q_0)^2\right] / I[|q_0^2|]}, \tag{19}$$

$$\ell_\infty(q) = \max|q_\tau - q_0| / \max|q_0|, \tag{20}$$

where I is an approximation to the global integral $I[x] = \sum x_j V_j$ and V_j is the volume associated with the value x_j. This computation is performed on the grid-interpolated data to facilitate volume computation.

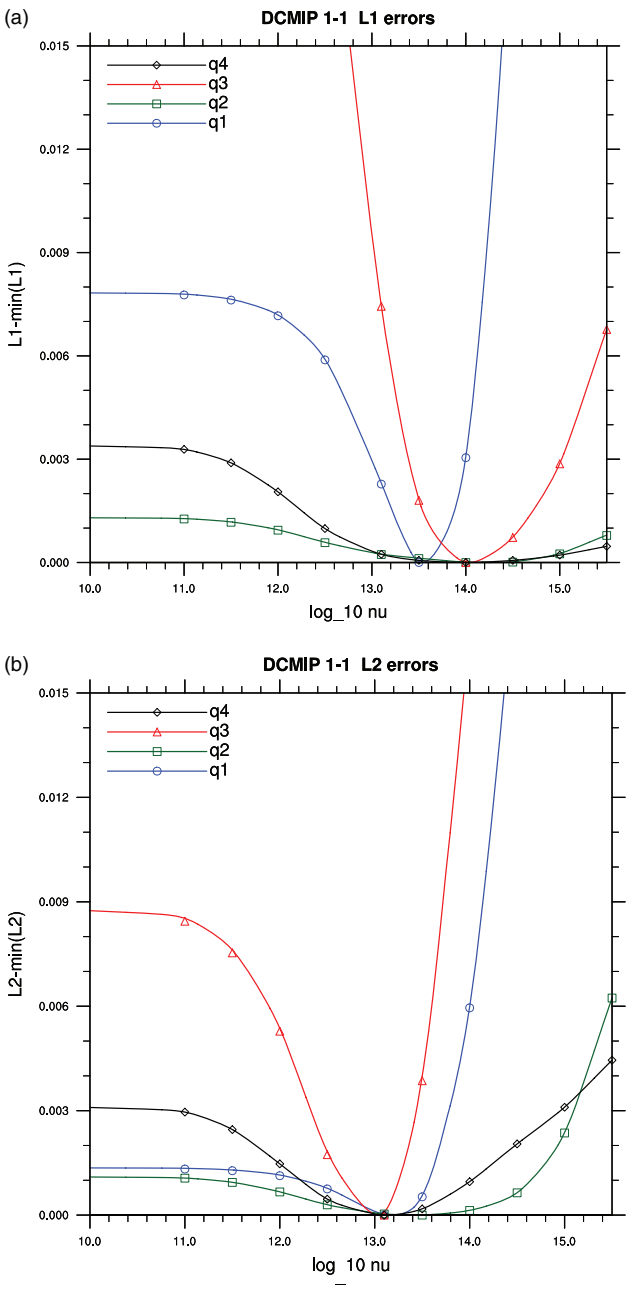

Figure 4. DCMIP 1-1 error norms versus hyperviscosity: (a) Vertically shifted error norms $\ell_1 - \min(\ell_1)$ are plotted for each tracer q_i as a function of hyperviscosity exponent $\mathcal{X} = \log_{10}(\nu)$. Minimum ℓ_1 error values are found in the range from $\mathcal{X} = 13.6$ to 14.0. (b) Vertically shifted error norms $\ell_2 - \min(\ell_2)$. Minimum ℓ_2 errors are found in the range from $\mathcal{X} = 13.0$ to 13.2.

Error norms for tracers q_1, q_3 and q_4 are presented in Table 3 at horizontal resolutions of $1^\circ \times 1^\circ$ ($N_p = 4$, $N_e = 30$) and 60 vertical levels, as recommended in the DCMIP test document. Error norms are also presented for CAM-FV and MCore, reproduced from Kent *et al.* (2014). Focusing on tracer q_1, we observe that error norms for CAM-SE are quite similar to those produced by MCore, but somewhat larger than those for CAM-FV. From this we conclude that CAM-FV's tracer transport does a little better at preserving smooth tracer distributions at the same resolution. For tracer q_3, the performance of all three dynamical cores was found to be comparable, with CAM-SE showing a small advantage.

3.1.4. *DCMIP 1-1 error norms versus hyperviscosity*

While hyperviscosity is not necessary for stability in linear tracer transport tests, it has the potential to influence the overall quality

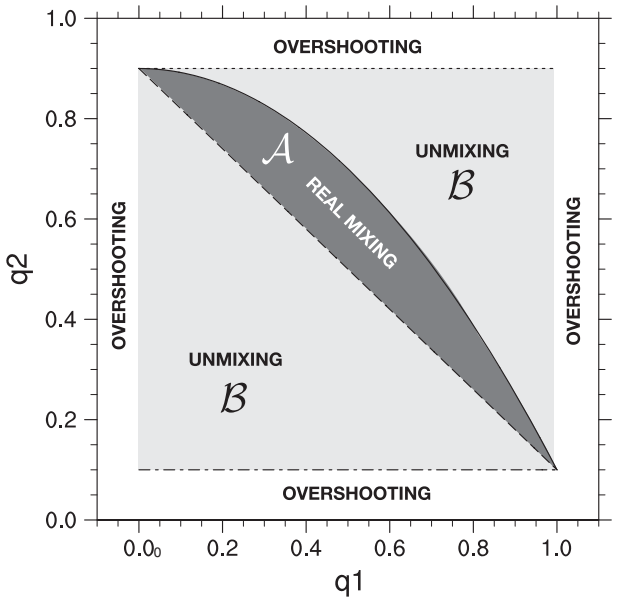

Figure 5. Tracer mixing regions. Region $\mathcal{A}$ is called the real-mixing region. Region $\mathcal{B}$ is the un-mixing region. The remaining area is the overshooting region.

of the solution. In order to isolate its impact, a parameter study was performed with no limiter applied and all other parameters held fixed. The time step was fixed at $\Delta t = 60$ s, and hyperviscosity was applied once per time step.

Figure 4(a) shows the ℓ_1 error for each tracer as a function of the hyperviscosity exponent $\mathcal{X}$, where $\nu = 10^{\mathcal{X}}\ \mathrm{m}^4\ \mathrm{s}^{-1}$ and (b) shows their ℓ_2 norms. In both plots, the curves have been vertically shifted by subtracting their minimum values to make it simpler to observe where each minimum occurs and how sensitive it is to $\mathcal{X}$.

From Figure 4, it is apparent that the use of hyperviscosity can improve the solution. However, no single hyperviscosity coefficient is optimal for all tracer configurations, and the optimum value of ℓ_1 differs from that of ℓ_2. For example, minimizing the ℓ_1 error for the double cosine bell q_1 requires $\mathcal{X} = 13.6$, while the slotted ellipsoid q_3 requires $\mathcal{X} = 14.0$. Optimizing ℓ_2 for tracer q_3, on the other hand, requires $\mathcal{X} = 13.0$, a full order of magnitude smaller. The ℓ_1 error is observed to be more sensitive to the parameter $\mathcal{X}$ than the ℓ_2 norm, as the optimal ℓ_2 errors are more tightly clustered with an optimal value for all tracers near $\mathcal{X} = 13.2$.

3.1.5. *Tracer correlations and mixing diagnostics*

Measurements of the numerical mixing that occurs during the simulation may be quantified using mixing diagnostics, which are described in Lauritzen and Thuburn (2012) and in the appendix of Kent *et al.* (2014). The mixing ratios q_2 and q_1 are plotted as a scatter plot obtained by sampling points in the five vertical levels closest to the heights of 4500, 4700, 4900, 5100, and 5300 m (levels 33–37 of 60, as measured from the top). Initially, the scatter points all fall on the line $q_2 = 0.9 - 0.8\,q_1^2$. At the end of the simulation, each of the points should remain on this line. Any deviation from this represents a loss of correlation between tracers 1 and 2.

Tracer correlation errors are classified by the region of the correlation plot in which they lie, as illustrated in Figure 5. Points that lie in region $\mathcal{A}$ (under the curve but above the dotted line) represent values that resemble 'real mixing'. Points that lie outside of region $\mathcal{A}$ but still within the box bounding the initial range $q_1 \in [0, 1]$, $q_2 \in [0.1, 0.9]$ lie in region $\mathcal{B}$, and are said to exhibit 'range-preserving un-mixing'. Points that lie outside of that box are said to be 'overshooting'.

The correlation errors are quantified by computing diagnostics for the real mixing error ℓ_r, range-preserving un-mixing ℓ_u, overshooting ℓ_o, and the total mixing error ℓ_m, each of which represents an area-weighted distance from the original curve. They are computed as follows:

$$\ell_\mathrm{r} = \sum_k d_k \frac{\Delta A_k}{A} \quad \text{for all } (q_{1,k}, q_{2,k}) \in \mathcal{A}, \tag{21}$$

$$\ell_\mathrm{u} = \sum_k d_k \frac{\Delta A_k}{A} \quad \text{for all } (q_{1,k}, q_{2,k}) \in \mathcal{B}, \tag{22}$$

$$\ell_\mathrm{o} = \sum_k d_k \frac{\Delta A_k}{A} \quad \text{for all } (q_{1,k}, q_{2,k}) \notin \mathcal{A} \cup \mathcal{B}, \tag{23}$$

$$\ell_\mathrm{m} = \ell_\mathrm{r} + \ell_\mathrm{u} + \ell_\mathrm{o}, \tag{24}$$

where d_k is the normalized minimum distance from the point $(q1_k, q2_k)$ to the original distribution curve. The value A represents the total area of the domain, and ΔA_k represents the area associated with sample point k. To provide simple area weighting, the diagnostics are computed from lat–lon interpolated values.

Figure 6 shows an analysis of the DCMIP 1-1 tracer correlations as a function of hyperviscosity, at time $t = 12$ days at a fixed resolution of 1° . The shaded regions are scatter plots with q_2 on the y-axis and q_1 on the x-axis arranged with a hyperviscosity coefficient $\mathcal{X}$ that increases from left to right. Table 4 displays the mixing diagnostic measurements for each case. Values for CAM-FV and MCore are presented for comparison.

As the hyperviscosity exponent is increased, the distributions become smoother and the scatter points move toward the centre or 'real mixing' region. Real mixing may seem preferable to overshooting or un-mixing, but points in this region are still erroneous, as at the final time the original relationship $q_2 = 0.9 - 0.8\,q_1^2$ should be strictly maintained. Minimizing the total area-weighted mixing error ℓ_m gives the best overall solution at $\mathcal{X} = 14.0$ with a value of $\ell_\mathrm{m} = 4.70 \times 10^{-3}$. These results are similar to those reported for MCore, but not as good as the results reported for CAM-FV.

3.1.6. *DCMIP 1-1 mixing error versus hyperviscosity*

Mixing diagnostics were measured as a function of hyperviscosity and plotted in Figure 7(a). From this plot, it is clear that real-mixing error (blue) increases with greater hyperviscosity and un-mixing error (green) generally falls, although not as quickly. Overshooting (red) exhibits a minimum value close to $\mathcal{X} = 14.25$ and the solid black line represents the sum ℓ_m, or total mixing error, which is minimized at $\mathcal{X} = 14.0$.

Figure 7(b) shows total mixing error curves plotted for 1° simulations for both the default polynomial order ($N_\mathrm{p} = 4, N_\mathrm{e} = 30$) and for simulations with a higher horizontal polynomial order ($N_\mathrm{p} = 7, N_\mathrm{e} = 15$). We see that the higher-order solution is more accurate overall and less sensitive to low hyperviscosity, as reducing the hyperviscosity by several orders of magnitude had little impact on the total mixing error. On the other hand, total mixing error rises rapidly in either case if too much hyperviscosity is applied.

3.2. *DCMIP test 1-2: Hadley-like meridional circulation*

DCMIP 1-2 is a tracer advection test that mimics a Hadley-like meridional circulation. It is similar to the test of Zerroukat and Allen (2012) but with time-reversal added to provide an analytical result for comparison. It is designed to investigate the impact of horizontal–vertical spatial splitting on the accuracy of the transport scheme. It uses the same isothermal temperature field as the previous test. The zonal, meridional and vertical velocity fields are prescribed to be

$$u = u_0 \cos\varphi, \tag{25}$$

$$v = -\frac{a w_0 \pi \rho_0}{K z_t \rho} \cos\varphi \sin(K\varphi)\ c_z\ c_t, \tag{26}$$

$$w = w_0 \frac{\rho_0}{K\rho} \{K \cos\varphi \cos(K\varphi) - 2 \sin\varphi \sin(K\varphi)\}\, s_z\, c_t, \tag{27}$$

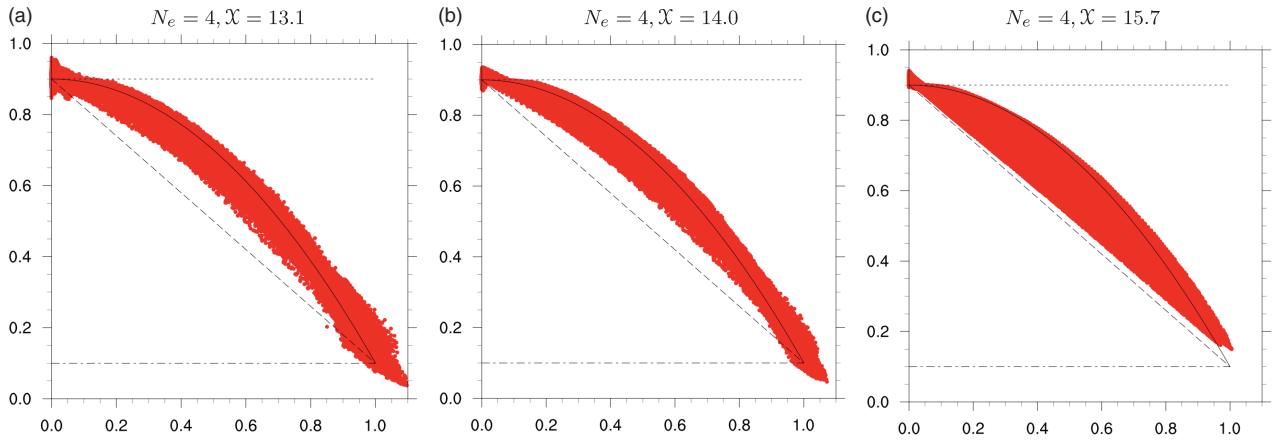

Model	ℓ_r	ℓ_u	ℓ_o	ℓ_m	hyperviscosity
CAM-SE	1.83×10^{-3}	1.98×10^{-3}	2.22×10^{-3}	6.04×10^{-3}	$\mathcal{X} = 13.1$
	2.09×10^{-3}	1.20×10^{-3}	1.42×10^{-3}	4.70×10^{-3}	$\mathcal{X} = 14.0$
	6.22×10^{-3}	0.76×10^{-3}	2.03×10^{-3}	9.00×10^{-3}	$\mathcal{X} = 15.7$
CAM-FV	1.04×10^{-3}	0.29×10^{-3}	0.0	1.33×10^{-3}	
MCore	2.53×10^{-3}	0.56×10^{-3}	1.08×10^{-3}	4.17×10^{-3}	

Figure 6. DCMIP 1-1 tracer correlation plots and normalized errors for tracer fields at $t = 12$ days. Red areas are scatter plots of q_2 versus q_1. The curved line represents the initial relationship $q_2 = 0.9 - 0.8q_1^2$. Increasing the hyperviscosity exponent from (a) 13.1 to (b) 14.0 to (c) 15.7 reduces the un-mixing error ℓ_u at the expense of increasing the real-mixing error u_r. [$\Delta x = 1^\circ, N_p = 4, N_e = 30, \Delta t = 60$ s, no limiter.]

Table 4. Mixing diagnostic measurements ℓ_r, ℓ_u, ℓ_o and ℓ_m (all $\times 10^{-3}$) and hyperviscosity $\mathcal{X}$.

Model	ℓ_r	ℓ_u	ℓ_o	ℓ_m	$\mathcal{X}$
CAM-SE	1.83	1.98	2.22	6.04	13.1
	2.09	1.20	1.42	4.70	14.0
	6.22	0.76	2.03	9.00	15.7
CAM-FV	1.04	0.29	0.00	1.33	
MCore	2.53	0.56	1.08	4.17	

where $\rho_0 = p_0/(R_d T_0)$ is the density at the surface, $c_z = \cos(\pi z/z_t)$, $c_t = \cos(\pi t/\tau)$, and $s_z = \sin(\pi z/z_t)$. Table 5 summarizes the various parameters in these equations.

The tracer field q_1 consists of a single horizontal layer spanning the globe between a height of z_1 and z_2 (m) such that

$$q_1 = \begin{cases} \frac{1}{2}\left\{1+\cos\left(\frac{2\pi(z-z_0)}{z_2-z_1}\right)\right\} & \text{if } z_1 < z < z_2, \\ 0 & \text{otherwise.} \end{cases} \tag{28}$$

As specified by the DCMIP test case document, simulations were performed at three resolutions: $2^\circ \times 2^\circ$ with 30 vertical levels (2° L30), $1^\circ \times 1^\circ$ with 60 vertical levels (1° L60), and $0.5^\circ \times 0.5^\circ$ with 120 vertical levels (0.5° L120). The vertical levels are evenly spaced in z, and the η levels are given by $\eta = \exp(-z/H)$. These simulations were performed using the quasi-monotonic limiter and no hyperviscosity.

Figure 8 shows vertical cross-sections of the tracer q_1 at time $t = 12$ h and $t = 24$ h at all three resolutions. From the 2° L30 cross-section, it is evident that gaps appear in the solution at $t = 12$ h where the tracer field is highly stretched and under-resolved by the grid (Figure 8(a)). At $t = 24$ h (Figure 8(b)), gaps remain in the solution in regions close to 30°N and 30°S, which is similar to results produced by the CAM-FV and MCore models. However, at the 1° L60 resolution (Figure 8(c, d)), the gapping is already greatly reduced, and appears to be less significant than that found in the other two models. At 0.5° L120 (Figure 8(e, f)) the tracer field is fully resolved throughout the simulation and the distortions at 30°N and 30°S have been nearly eliminated.

Figure 9 displays error norms produced by DCMIP test 1-2 computed by comparison of the initial and final tracer distributions. Table 7 displays CAM-SE error norms measured with and without the quasi-monotonic limiter at the default polynomial order $N_p = 4$, as well as error norms for a high-order configuration $N_p = 7$. Results from the CAM-FV and MCore models are also reproduced from Kent *et al.* (2014) to facilitate comparison.

At 1°, ℓ_1 and ℓ_2 errors of CAM-SE were somewhat smaller than those of CAM-FV and generally similar to those produced by MCore for this test. The high-order configuration $N_p = 7$ exhibited somewhat greater accuracy than the $N_p = 4$ configuration, particularly at the coarsest resolution $\Delta x = 2^\circ$.

The rightmost column of Table 7 shows the error convergence rates obtained by averaging rates for $2^\circ \rightarrow 1^\circ$ and $1^\circ \rightarrow 0.5^\circ$. The error convergence rate for each norm was found to be close to 2, confirming that the model exhibits second-order accuracy for this test. To obtain a more precise measurement of the order, a grid-size refinement study was performed for the $N_p = 4$ configurations using multiple resolutions ranging from 2° to 0.5°, as plotted in Figure 9.

A least-squares linear fit shows that the ℓ_1 error converges under grid-size refinement at a rate of $\mathcal{O}(\Delta x^{2.32})$ when no limiter is applied and a small $\Delta t = 5$ s time step is used. Application of the quasi-monotonic limiter reduced the convergence rate to $\mathcal{O}(\Delta x^{2.18})$. Increasing the time step to $\Delta t = 60$ reduced the order still further as the time-discretization error began to dominate the spatial-discretization errors at resolutions finer than 1°.

To determine if second-order accuracy was impacted by level spacing, the convergence study was repeated using equally spaced η levels rather than equally spaced z levels. This arrangement produces levels that are packed more tightly at the bottom of the atmosphere than at the top. These simulations exhibited an error that was roughly 25% smaller, at the same resolution. However, the ℓ_1 error exhibited the same $\mathcal{O}(\Delta x^{2.3})$ order of convergence under grid refinement.

3.3. *DCMIP 1-3: thin cloud advection over orography*

DCMIP 1-3 investigates the influence of orography on tracer advection. Several thin cloud-like layers are transported laterally

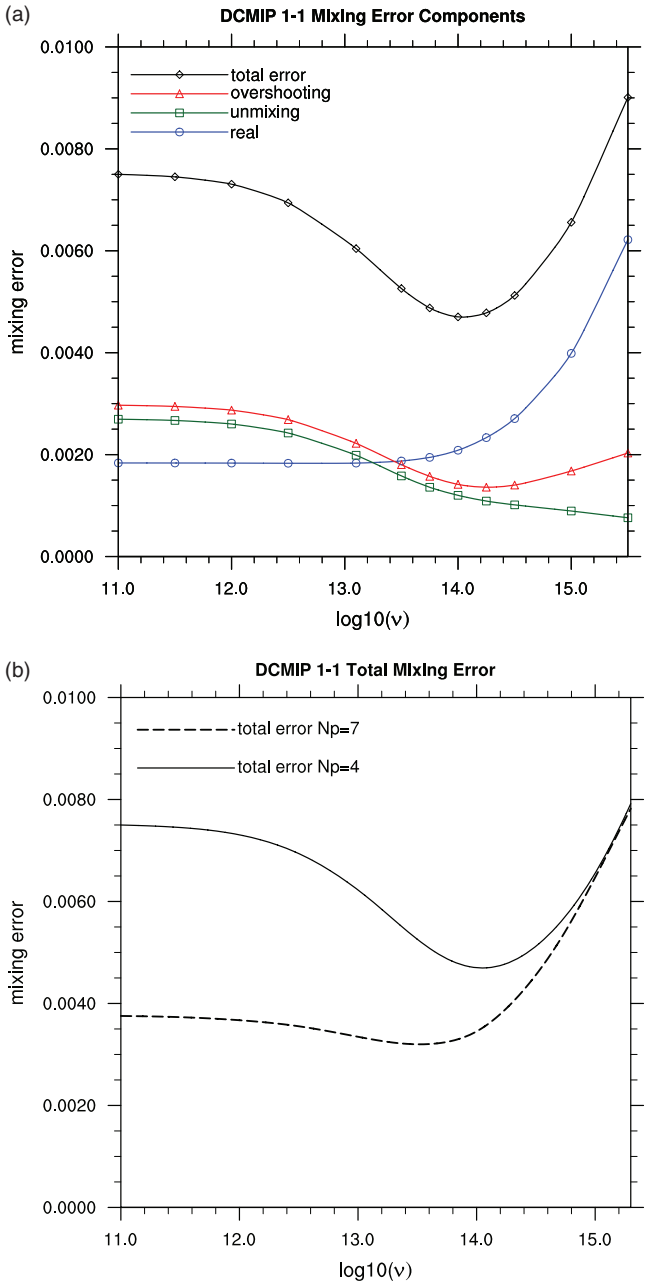

Figure 7. DCMIP 1-1 Mixing diagnostics versus hyperviscosity: (a) Mixing diagnostics as a function of the hyperviscosity exponent $\mathcal{X} = \log_{10}(\nu)$ for $N_e = 30$, $N_p = 4$, $\Delta x = 1^\circ$. Adding hyperviscosity reduces un-mixing error ℓ_u but increases real-mixing error ℓ_r. The overshooting error l_u is minimal at $\mathcal{X} = 14.25$ and the total mixing error is minimized at $\mathcal{X} = 14$ with $\ell_m = 4.70 \times 10^{-3}$. (b) Total mixing error is compared for $N_p = 4$ and $N_p = 7$, both at $\Delta x = 1^\circ$. The higher-order simulation exhibits a lower minimum mixing error of $\ell_m = 3.22 \times 10^{-3}$ and requires a smaller hyperviscosity exponent of $\mathcal{X} = 13.5$.

across the globe, completing one orbit in a period of $\tau = 12$ days. As with the previous tests, an isothermal atmosphere is employed with a temperature $T_0 = 300$ K. The zonal, meridional, and vertical wind speed components are

$$u = u_0 \left(\cos\varphi \cos\alpha + \sin\varphi \cos\lambda \sin\alpha\right), \tag{29}$$

$$v = -u_0 \sin\lambda \sin\alpha, \tag{30}$$

$$w = 0, \tag{31}$$

describing 'solid-body' rotation with the rotation axis tilted at an angle of $\alpha = 30^\circ$ from the Earth's axis of rotation.

Due to the use in CAM-SE of hybrid terrain-following vertical coordinates, horizontal motion produces an effective vertical flux causing the tracers to pass through several vertical η levels. This flux is related to the vertical pressure-velocity ω through its material derivative such that

$$\omega = \frac{\partial p_s}{\partial t} + \boldsymbol{u}\nabla_\eta p + \dot{\eta}\frac{\partial p}{\partial \eta}.$$

Using $\partial p_s/\partial t = 0$ and $\omega = 0$, the vertical flux needed for tracer transport is simply

$$\dot{\eta}\frac{\partial p}{\partial \eta} = -\boldsymbol{u} \cdot \nabla_\eta p. \tag{32}$$

The influence of the terrain-following coordinates is more pronounced in regions with steeper orography. Some relevant parameters for DCMIP test 1-3 are listed in Table 6. The full description of the initial conditions is provided in Kent *et al.* (2014).

For this test, the surface elevation is

$$z_s = \begin{cases} \dfrac{h_0}{2}\left\{1+\cos\left(\pi\dfrac{r_m}{R_m}\right)\right\}\cos^2\left(\pi\dfrac{r_m}{\zeta_m}\right) & \text{if } r_m < R_m, \\ 0 & \text{otherwise,} \end{cases} \tag{33}$$

where r_m is the great-circle distance on the unit sphere measured from the centre of the mountain range at $(\lambda_m = 3\pi/2, \varphi_m = 0)$. This equation describes a Schär-type mountain range (Schär *et al.*, 2002) with steep mountains that decay in height over a distance R_m.

Three tracer fields are used to simulate thin cloud layers, stacked vertically at different heights. Tracer layers q_1 and q_2 are disc-shaped and the upper layer q_3 is cylindrical. Tracer q_4 is the sum of the other three. Figure 10 provides a three-dimensional view of the initial tracer configuration and surface orography.

Layer interfaces are placed at evenly spaced heights z_i (in the flat region) spanning an altitude of $z_s = 0$ to $z_t = 12\,000$ m. The η_i interfaces are then chosen to match those levels in the mountain-free region such that

$$\eta_i = \mathrm{e}^{-z_i/H}, \quad B_i = \left[\frac{\eta_i - \eta_t}{1-\eta_t}\right]^c, \quad A_i = \eta_i - B_i. \tag{34}$$

The smoothing exponent c controls the rate at which η transforms from a terrain-following coordinate to a pure pressure coordinate with height, with a default value of $c = 1$ for this test. The horizontal resolution for all runs was fixed at 1° with $L = 30$, 60, or 120 vertical levels. The time step was $\Delta t = 100$ s, with the quasi-monotonic limiter, and no hyperviscosity.

Figure 11 displays an equatorial vertical cross-section of tracer field q_4 at time $t = 0$, 6 and 12 days. (d,e,f) display q_4 in longitude versus η coordinates and (a,b,c) display longitude versus z. Surfaces of constant η (grey) appear as simple horizontal lines in η coordinates and highly oscillatory lines in z.

The terrain-following coordinates cause significant distortion of the tracer field over the mountainous region, as seen in Figure 11(e) at time $t = 6$ days. Comparing the final state at $t = 12$ days with the initial state, we observe that the horizontal tracer distribution has been well preserved, while the vertical

Table 5. Some constants used in test 1-2.

Parameter	Value	Description
K	5	Number of overturning cells
p_t	254.944 hPa	Pressure at the model top
p_0	1000 hPa	Reference pressure
T_0	300 K	Isothermal temperature
u_0	40 m s^{-1}	Reference zonal velocity
w_0	0.15 m s^{-1}	Reference vertical velocity
z_1	2000 m	Lower boundary of tracer layer
z_2	5000 m	Upper boundary of tracer layer
z_t	12 000 m	Height of model top
τ	1 day	Period of motion

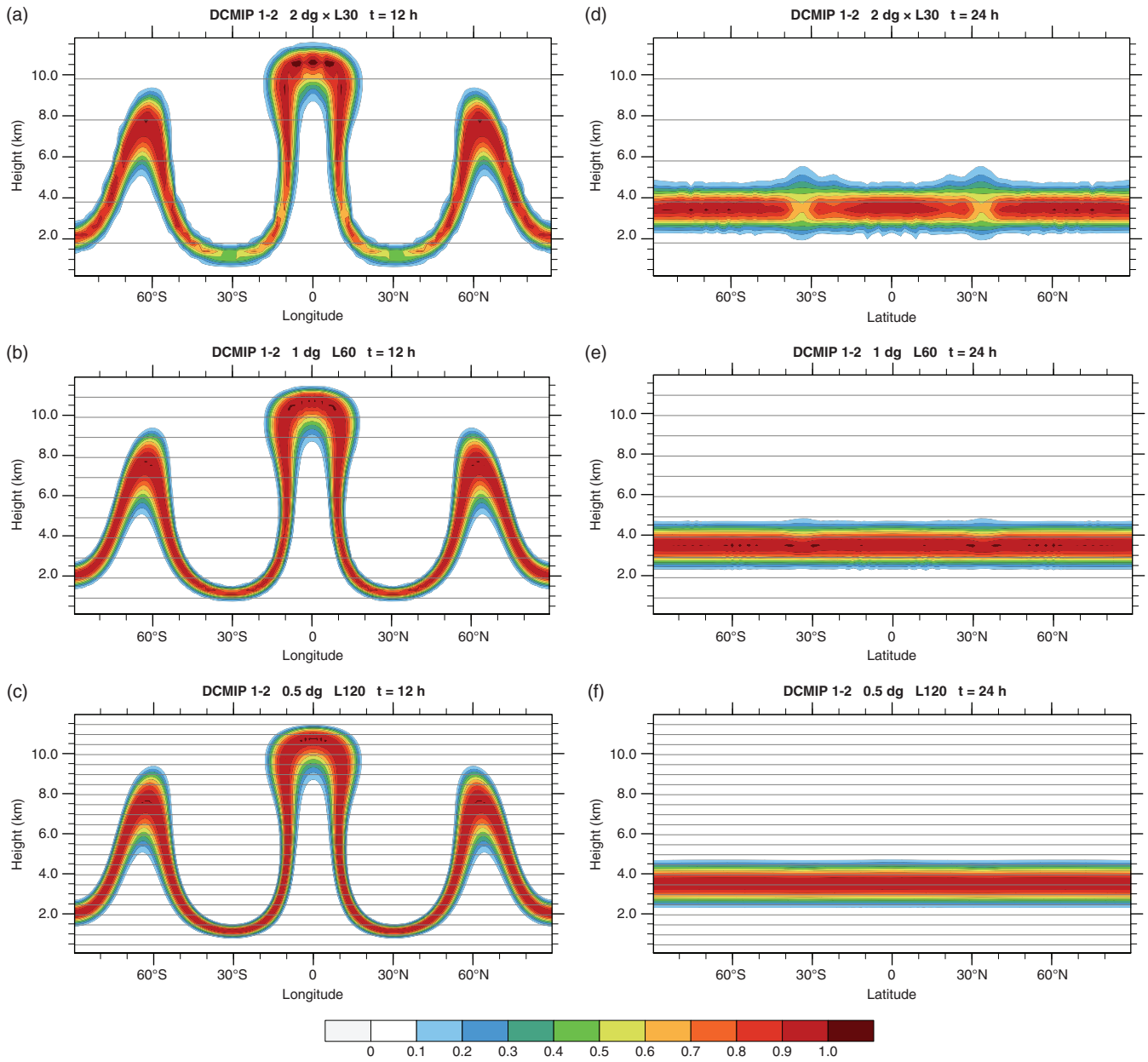

Figure 8. DCMIP 1-2. Latitude–height cross-sections of q_1 at (a, c, e) $t = 12$ h and (b, d, f) $t = 24$ h at longitude $\lambda = 180°$. At (a, b) 2° resolution, the simulation is not fully resolved and gapping is visible in the highly stretched regions near $\varphi = 30°$S and 30°N. At (e, f) 0.5° resolution the simulation is fully resolved and the gapping has mostly been eliminated. [$\Delta t = 60, \nu = 0, N_p = 4$, quasi-monotone limiter]

distribution exhibits moderate diffusion and distortion. The magnitude of the distortion is smaller for the higher cloud layers, as the η coordinates are less oscillatory near the top of the domain. The results look somewhat better than those of CAM-FV and are similar to those of MCore.

Table 8 shows the error norms for test 1-3 runs with vertical resolutions of 30, 60, and 120 levels ($\Delta z = 400, 200$, and 100 m grid spacing), with a fixed lateral resolution of 1°. Using the default value of $c = 1$ we observe CAM-SE error norms that are somewhat smaller than CAM-FV and somewhat larger than MCore. Increasing the smoothing coefficient to $c = 2$ reduces the errors significantly, indicating a high sensitivity to this parameter. The right-hand columns indicate that CAM-SE exhibits error convergence rates below first-order under vertical level refinement, which is consistent with the other two models. Overall, it is clear that models using terrain-following coordinates have difficulty producing accurate results in the presence of steep, rapidly oscillating orography.

Although increasing the vertical resolution produces little benefit in this test, the accuracy of the solution may be enhanced by reducing the impact of the orography. In Figure 12, the ℓ_1 error is plotted as a function of the vertical smoothing exponent c. As the value of c is increased, the impact of the orography becomes more strongly confined to the lower levels, thereby reducing the errors in the upper atmosphere. By examining the green line representing the ℓ_1 error for $L = 60$, one can see that increasing the smoothing exponent from $c = 1$ to $c = 3.5$ reduces the error by roughly a factor of 3. Increasing c beyond 3.5 began to adversely impact the maximum stable time step and the stability of the vertical remap algorithm.

4. Conclusions

The DCMIP 1-*x* tracer transport tests were performed by applying the advection routines of CAM-SE with all other dynamic routines suppressed. The default tracer scheme was used, which employs spectral elements in the horizontal and second-order Lagrangian transport with remap in the vertical.

The DCMIP 1-1 test examines several tracers with strong horizontal deformation and vertical oscillation. At the final time of $t = 12$ days, the tracer distributions were found to be reasonably well preserved with some diffusion of sharp features. Error norms were generally similar to those produced by CAM-FV and MCore. CAM-SE exhibited somewhat better error norms for

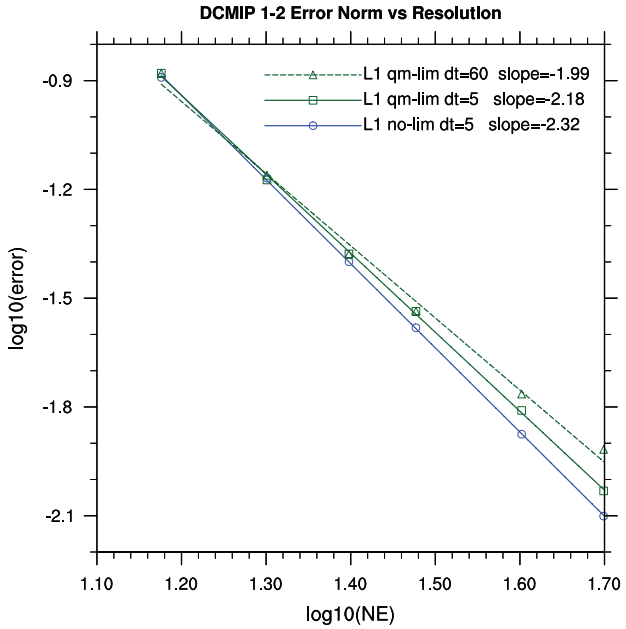

Figure 9. DCMIP 1-2: Error convergence under grid refinement The convergence rate is computed more accurately by a grid-size refinement study where NE is the number of elements per cubed-sphere face, which reveals that for $N_p = 4$, the ℓ_1 error converges at $\mathcal{O}(\Delta x^{2.3})$. The order is reduced slightly when the quasi-monotonic limiter is applied, and when large time steps are used.

Table 6. Some constants used in test 1-3.

Parameter	Value	Description
h_0	2000 m	Mountain-range height
p_t	254.944 hPa	Pressure at model top
R_m	$3\pi/4$ rad	Mountain-range radius
T_0	300 K	Isothermal temperature
u_0	$2\pi a/\tau$	Maximum wind speed
z_t	12000 m	Model top
$z_{p,1}$	3050 m	Altitude of cloud 1
$z_{p,2}$	5050 m	Altitude of cloud 2
$z_{p,3}$	8200 m	Altitude of cloud 3
$\Delta z_{p,1}$	1000 m	Thickness of cloud 1
$\Delta z_{p,2}$	1000 m	Thickness of cloud 2
$\Delta z_{p,3}$	1000 m	Thickness of cloud 3
α	$\pi/6$ rad	Advection angle
ζ_m	$\pi/16$ rad	Mountain oscillation half-width
τ	12 days	Period of motion

Table 7. DCMIP 1-2: Error versus resolution. Tracer error norms are shown for each solver at low, medium, and high resolutions, along with the average convergence rate for each norm. Roughly second-order accuracy is observed for CAM-SE.

	Norm	2° L30	1° L60	0.5° L120	Rate
CAM-SE	ℓ_1	0.1320	0.0291	0.0100	1.86
$N_p = 4$	ℓ_2	0.1448	0.0322	0.0122	1.79
qm-limiter	ℓ_∞	0.3796	0.0977	0.0461	1.52
CAM-SE	ℓ_1	0.1255	0.0262	0.0054	2.27
$N_p = 4$	ℓ_2	0.1374	0.0288	0.0073	2.12
no limiter	ℓ_∞	0.3857	0.1977	0.0373	1.68
CAM-SE	ℓ_1	0.0906	0.0200	0.0047	2.13
$N_p = 7$	ℓ_2	0.0856	0.0261	0.0071	1.80
no limiter	ℓ_∞	0.5196	0.0842	0.0306	2.04
	ℓ_1	0.1810	0.0411	0.0124	1.93
CAM-FV	ℓ_2	0.2047	0.0536	0.0159	1.84
	ℓ_∞	0.4705	0.1575	0.0473	1.66
	ℓ_1	0.1368	0.0286	0.0063	2.22
MCore	ℓ_2	0.1659	0.0462	0.0113	1.94
	ℓ_∞	0.4214	0.1586	0.0435	1.64

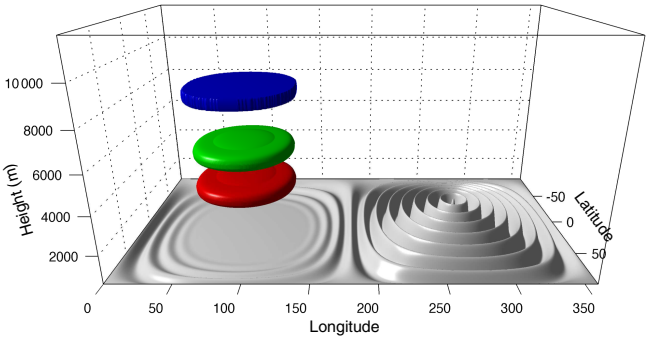

Figure 10. DCMIP 1-3: Tracer and orography isosurfaces. The $q = 0.01$ isosurfaces are plotted for the initial conditions for tracers q_1 (red), q_2 (green), q_3 (blue) and surface elevation z_s (grey) at $t = 0$. Tracers fields q_1 and q_2 are disc shapes, while q_3 is cylindrical. Tracer q_4 is the sum of all three. At the surface a rapidly oscillating Schär-type mountain range is employed with a maximum mountain height of $z = 2000$ m.

the slotted ellipsoid distribution q_3. CAM-FV exhibited somewhat better error norms for the double cosine bell distribution q_1. Error regression on the hyperviscosity parameter ν revealed no single optimal value. Rather, each tracer configuration and error norm had a slightly different optimum. Optimal ℓ_2 norms were obtained in the range $\nu = 10^{13}$ to $10^{13.2}\,\mathrm{m^4\,s^{-1}}$. Optimal ℓ_1 norms were obtained in the range $\nu = 10^{13.6}$ to $10^{14}\,\mathrm{m^4\,s^{-1}}$. Minimal mixing error was obtained at $\nu = 10^{14}$. Mixing errors were comparable with those reported for MCore, but were not as good as CAM-FV. At fixed resolution and time step, increasing the polynomial order to $N_p = 7$ was found to improve the accuracy and reduce the sensitivity of the mixing error to hyperviscosity.

DCMIP 1-2 examines horizontal–vertical coupling in a Hadley-like circulation. Vertical cross-sections were similar to those of CAM-FV and MCore, with some tracer gapping occurring near 30°N and 30°S. At the default resolution $N_p = 4$, error norms were found to be smaller than CAM-FV and similar to MCore. The high-resolution configuration $N_p = 7$ produced a small improvement over $N_p = 4$. Error convergence under simultaneous grid-size refinement of the horizontal and vertical grid was also studied. The ℓ_1 norm converged with order 2.3 with no limiter applied and with order 2.2 with the quasi-monotonic limiter.

DCMIP test 1-3 examines the effects of terrain-following coordinates on thin tracer clouds. The error norms produced by CAM-SE were a little better than CAM-FV and a little worse than those of MCore. Vertical refinement, with horizontal resolution held fixed, produced little to no improvement in the error as increasing the number of vertical layers increases accuracy but also increases the distortion due to flux between the layers. However, it was possible to significantly improve the accuracy of the simulation by increasing the smoothing exponent, thereby reducing the impact of the terrain-following coordinates on the upper atmospheric levels.

Overall the default tracer transport scheme in CAM-SE exhibited error norms comparable to CAM-FV and MCore on all three tests. The scheme was verified to achieve second-order accuracy with or without limiting. However, the quasi-monotonic limiter was unable to maintain strict monotonicity of the mixing ratio for these tests, most likely due to mass–wind inconsistency, a problem which is common to prescribed-velocity scenarios. As with the other dynamical cores, horizontal transport of thin tracer clouds over a Schär mountain range was found to be particularly challenging due to the numerical mixing caused by terrain-following coordinates. A number of new techniques are being actively developed in the CAM-SE context, including high-order vertical representations, discontinuous-Galerkin methods, semi-Lagrangian transport schemes, and alternate boundary implementations, each of which has the potential to improve upon these results.

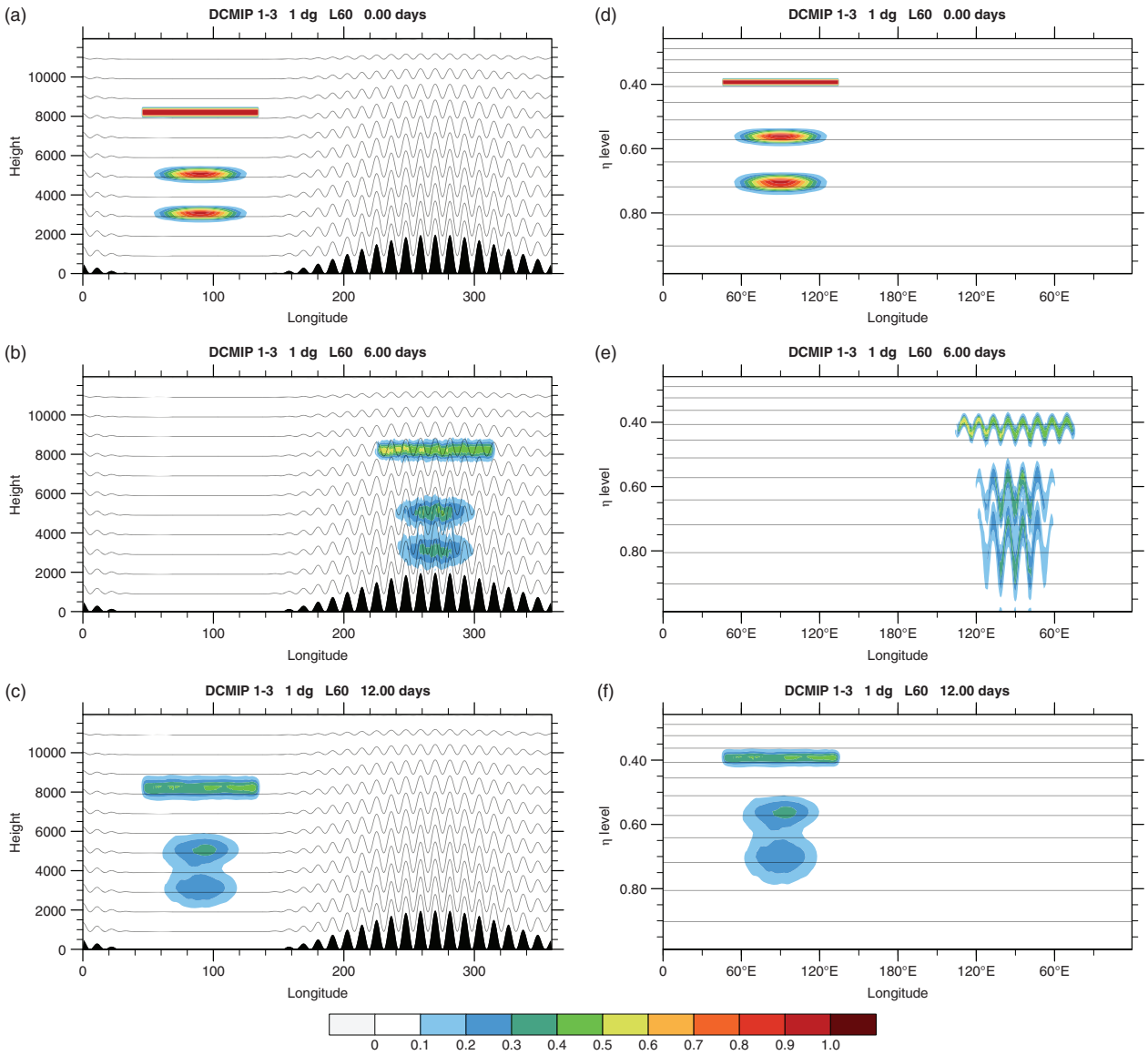

Figure 11. DCMIP 1-3: Vertical cross-sections of the tracer field q_4 are plotted at (a, b) $t = 0$ days, (c, d) 6 days and (e, f) 12 days on a 1° grid with 60 vertical levels ($\Delta z = 200$ m). Thin cloud-like tracers fields are transported horizontally over rapidly oscillating orography causing them to interact with the terrain-following vertical levels. (a,b,c) show the tracer in z-coordinate space, and (d,e,f) are plotted in η-coordinate space. As the tracers cross the mountain, vertical oscillation is induced between the η levels, which produces some distortion. [$\Delta x = 1°, N_p = 4, N_e = 30, \Delta t = 100, \nu = 0, c = 1$, quasi-monotone limiter]

Acknowledgements

We would like to acknowledge Ben Jamroz, Colin Zarzycki, Mike Levy, and Alexandra Jahn for their helpful feedback and useful discussions. This work was supported by the DOE BER SciDAC grant DE-SC 0006959: 'A petascale non-hydrostatic atmospheric dynamical core in the HOMME framework'. CJ was supported by the DOE Office of Science grants DE-SC0003990 and DE-SC0006684. Computational resources were provided by the Extreme Science and Engineering Discovery Environment (XSEDE), which is supported by National Science Foundation grant number ACI-1053575.

Table 8. DCMIP 1-3: Normalized errors for the tracer field q_4 at $t = 12$ days and the average convergence rate for each norm. Simulation parameters: [$\Delta x = 1°, N_p = 4, N_e = 30, \Delta t = 100$ s, $\nu = 0$, quasi-monotonic limiter.]

		Normalized error			Convergence rate		
	Norm	1° L30	1°L60	1°L120	L30→L60	L60→L120	Average
CAM-SE	ℓ_1	0.90	0.53	0.42	0.78	0.33	0.55
	ℓ_2	0.56	0.35	0.32	0.68	0.13	0.41
($c = 2$)	ℓ_∞	0.72	0.63	0.70	0.20	−0.17	0.02
CAM-SE	ℓ_1	1.25	1.12	1.11	0.15	0.13	0.08
	ℓ_2	0.75	0.68	0.68	0.14	−0.0072	0.07
($c = 1$)	ℓ_∞	0.92	0.91	0.88	0.02	0.0039	0.03
CAM-FV	ℓ_1	1.35	1.33	1.31			
	ℓ_2	0.81	0.77	0.78			
	ℓ_∞	0.88	0.85	0.91			
MCore	ℓ_1	1.08	0.89	0.83			
	ℓ_2	0.70	0.57	0.55			
	ℓ_∞	0.81	0.71	0.73			

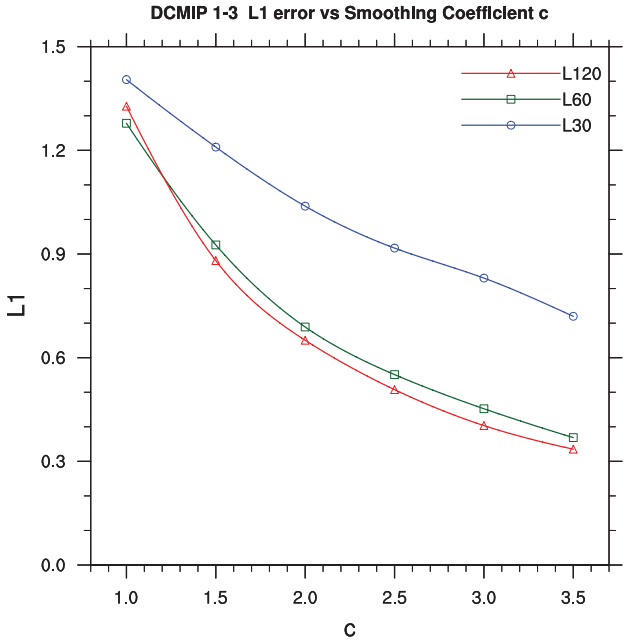

Figure 12. Test 1-3: ℓ_1 error versus smoothing exponent c is displayed for vertical resolutions $L = 30$, 60, and 120 at day 12. Increasing the value of c reduces the impact of the orography on the upper levels, thereby improving the accuracy. [$\Delta x = 1^\circ, N_p = 4, N_e = 30, \Delta t = 60\,\text{s}, \nu = 0$, no limiter.]

References

Dennis J, Edwards J, Evans KJ, Guba ON, Lauritzen PH, Mirin AA, St-Cyr A, Taylor MA, Worley PH. 2012. CAM-SE: A scalable spectral element dynamical core for the community atmosphere model. *Int. J. High Perform. Comput. Appl.* **26**: 74–89, doi: 10.1177/1094342011428142.

Deville MO, Fischer PF, Mund EH. 2002. *High-Order Methods for Incompressible Fluid Flow*. Cambridge University Press: Cambridge, UK.

Erath C, Nair RD. 2014. A conservative multi-tracer transport scheme for spectral-element spherical grids. *J. Comput. Phys.* **256**: 118–134.

Gates WL. 1992. AMIP: The atmospheric model intercomparison project. *Bull. Am. Meteorol. Soc.* **73**: 1962–1970.

Gates WL, Boyle JS, Covey C, Dease CG, Doutriaux CM, Drach RS, Fiorino M, Gleckler PJ, Hnilo JJ, Marlais SM, Phillips TJ, Potter GL, Santer BD, Sperber KR, Taylor KE, Williams DN. 1999. An overview of the results of the Atmospheric Model Intercomparison Project (AMIP I). *Bull. Am. Meteorol. Soc.* **80**: 29–55.

Guba O, Taylor M, St-Cyr A. 2014. Optimization-based limiters for the spectral element method. *J. Comput. Phys.* **267**: 176–195.

Hurrell JW, Holland M, Gent P, Ghan S, Kay JE, Kushner P, Lamarque JF, Large W, Lawrence D, Lindsay K, Lipscomb WH, Long MC, Mahowald N, Marsh DR, Neale RB, Rasch P, Vavrus S, Vertenstein M, Bader D, Collins WD, Hack JJ, Kiehl J, Marshall S. 2013. The Community Earth System Model: A framework for collaborative research. *Bull. Am. Meteorol. Soc.* **94**: 1339–1360.

Jablonowski C, Ullrich PA, Kent J, Reed KA, Taylor MA, Lauritzen PH, Nair RD. 2012. 'The 2012 dynamical core model intercomparison project (DCMIP)'. In: AGU Fall Meeting Abstracts, A53C-0160. http://fallmeeting.agu.org/2012/files/2012/12/AGU_poster_Jablonowski_Dec_2012.pdf (accessed 3 July 2016).

Jöckel P, von Kuhlmann R, Lawrence MG, Steil B, Brenninkmeijer CAM, Crutzen PJ, Rasch PJ, Eaton B. 2001. On a fundamental problem in implementing flux-form advection schemes for tracer transport in three-dimensional general circulation and chemistry transport models. *Q. J. R. Meteorol. Soc.* **127**: 1035–1052, doi:10.1002/qj.49712757318.

Karniadakis G, Sherwin S. 2013. *Spectral/hp Element Methods for Computational Fluid Dynamics*. Oxford University Press: Oxford, UK.

Kasahara A. 1974. Various vertical coordinate systems used for numerical weather prediction. *Mon. Weather Rev.* **102**: 509–522.

Kent J, Ullrich PA, Jablonowski C. 2014. Dynamical core model intercomparison project: Tracer transport test cases. *Q. J. R. Meteorol. Soc.* **140**: 1279–1293, doi: 10.1002/qj.2208.

Lauritzen PH, Thuburn J. 2012. Evaluating advection/transport schemes using interrelated tracers, scatter plots and numerical mixing diagnostics. *Q. J. R. Meteorol. Soc.* **138**: 906–918.

Lauritzen PH, Nair RD, Ullrich PA. 2010. A conservative semi-Lagrangian multi-tracer transport scheme (CSLAM) on the cubed-sphere grid. *J. Comput. Phys.* **229**: 1401–1424.

Lin SJ. 2004. A 'vertically Lagrangian' finite-volume dynamical core for global models. *Mon. Weather Rev.* **132**: 2293–2307.

Meehl GA, Boer GJ, Covey C, Latif M, Stouffer RJ. 2000. The Coupled Model Intercomparison Project (CMIP). *Bull. Am. Meteorol. Soc.* **81**: 313–318.

Meehl G, Covey C, McAvaney B, Latif M, Stouffer R. 2005. Overview of the Coupled Model Intercomparison Project (CMIP). *Bull. Am. Meteorol. Soc.* **86**: 89–93.

Nair RD, Lauritzen PH. 2010. A class of deformational flow test cases for linear transport problems on the sphere. *J. Comput. Phys.* **229**: 8868–8887.

Nair R, Choi HW, Tufo H. 2009. Computational aspects of a scalable high-order discontinuous Galerkin atmospheric dynamical core. *Computers & Fluids* **38**: 309–319.

Nair RD, Bao L, Toy MD. 2015. A time-split discontinuous Galerkin transport scheme for global atmospheric model. *Procedia Comput. Sci.* **51**: 2056–2065.

Neale RB, Chen CC, Gettelman A, Lauritzen PH, Park S, Williamson DL, Conley AJ, Garcia R, Kinnison D, Lamarque JF, Marsh D, Mills M, Smith AK, Tilmes S, Vitt F, Morrison H, Cameron-Smith P, Collins WD, Iacono MJ, Easter RC, Ghan SJ, Liu X, Rasch PJ, Taylor MJ. 2010. 'Description of the NCAR community atmosphere model (CAM 5.0)'. Technical Note NCAR/TN-486+STR. National Center for Atmospheric Research: Boulder, CO.

Rančić M, Purser R, Mesinger F. 1996. A global shallow-water model using an expanded spherical cube: Gnomonic versus conformal coordinates. *Q. J. R. Meteorol. Soc.* **122**: 959–982.

Reed KA, Jablonowski C. 2012. Idealized tropical cyclone simulations of intermediate complexity: A test case for AGCMs. *J. Adv. Model. Earth Sys.* **4**: M04 001, doi: 10.1029/2011MS000099.

Sadourny R. 1972. Conservative finite-difference approximations of the primitive equations on quasi-uniform spherical grids. *Mon. Weather Rev.* **100**: 136–144.

Schär C, Leuenberger D, Fuhrer O, Lüthi D, Girard C. 2002. A new terrain-following vertical coordinate formulation for atmospheric prediction models. *Mon. Weather Rev.* **130**: 2459–2480.

Simmons AJ, Burridge DM. 1981. An energy and angular-momentum conserving vertical finite-difference scheme and hybrid vertical coordinates. *Mon. Weather Rev.* **109**: 758–766.

Spiteri RJ, Ruuth SJ. 2002. A new class of optimal high-order strong-stability-preserving time discretization methods. *SIAM J. Numer. Anal.* **40**: 469–491.

Taylor MA, Cyr AS, Fournier A. 2009. A non-oscillatory advection operator for the compatible spectral element method. In *Computational Science-ICCS 2009*: 273–282. Springer: Berlin.

Thomas SJ, Loft RD. 2005. The NCAR spectral element climate dynamical core: Semi-implicit Eulerian formulation. *J. Sci. Comput.* **25**: 307–322.

Ullrich PA, Jablonowski C. 2012. MCore: A non-hydrostatic atmospheric dynamical core utilizing high-order finite-volume methods. *J. Comput. Phys.* **231**: 5078–5108.

Ullrich PA, Jablonowski C, Kent J, Lauritzen PH, Nair RD, Taylor MA. 2012. 'Dynamical Core Model Intercomparison Project (DCMIP) test case document', https://www.earthsystemcog.org/projects/dcmip-2012/ (accessed 21 February 2016).

Williamson DL, Drake JB, Hack JJ, Jakob R, Swarztrauber PN. 1992. A standard test set for numerical approximations to the shallow-water equations in spherical geometry. *J. Comput. Phys.* **102**: 211–224.

Zerroukat M, Allen T. 2012. A three-dimensional monotone and conservative semi-Lagrangian scheme (SLICE-3D) for transport problems. *Q. J. R. Meteorol. Soc.* **138**: 1640–1651.

